# Comparison of Earth rotation excitation in data-constrained and unconstrained atmosphere models

Lisa J. Neef[1,2] and Katja Matthes[1,2,3]

Received 13 July 2011; revised 4 November 2011; accepted 5 November 2011; published 25 January 2012.

[1] Changes in Earth rotation are strongly related to fluctuations in the angular momentum of the atmosphere, and therefore contain integral information about the atmospheric state. Here we investigate the extent to which observed Earth rotation parameters can be used to evaluate and potentially constrain atmospheric models. This is done by comparing the atmospheric excitation function, computed geophysically from reanalysis data and climate model simulations constrained only by boundary forcings, to the excitation functions inferred from geodetic monitoring data. Model differences are assessed for subseasonal variations, the annual and semiannual cycles, interannual variations, and decadal-scale variations. Observed length-of-day anomalies on the subseasonal timescale are simulated well by the simulations that are constrained by meteorological data only, whereas the annual cycle in length-of-day is simulated well by all models. Interannual length-of-day variations are captured fairly well as long as a model has realistic, time-varying SST boundary conditions and QBO forcing. Observations of polar motion are most clearly relatable to atmospheric dynamics on subseasonal to annual timescales, though angular momentum budget closure is difficult to achieve even for data-constrained atmospheric simulations. Closure of the angular momentum budget on decadal timescales is difficult and strongly dependent on estimates of angular momentum fluctuations due to core-mantle interactions in the solid Earth.

**Citation:** Neef, L. J., and K. Matthes (2012), Comparison of Earth rotation excitation in data-constrained and unconstrained atmosphere models, *J. Geophys. Res.*, *117*, D02107, doi:10.1029/2011JD016555.

## 1. Introduction

[2] The rotation and orientation of the Earth are not constant in time, but vary on a wide range of timescales. The gravity of the sun, moon, and other planets are external torques that deform the solid Earth, causing it to precess and nutate as it rotates. The angular momentum of the Earth is also changed by internal processes, and by the exchange of angular momentum between the Earth and its fluid shell, that is, the oceans, continental hydrosphere, and atmosphere. Exchange of angular momentum between these subsystems and the solid Earth changes the Earth's rate of rotation and the orientation of its rotational pole. The Earth rotation rate and polar motion (so-called Earth Rotation Parameters, or ERPs) have been measured since the late 19th century, and have achieved a high degree of precision since the advent of space geodetic observing techniques in the 1980s [*Gross*, 2009].

[3] Atmospheric angular momentum (AAM) in particular is a strong source of excitation of Earth rotation variations, and is the focus of this study. AAM varies due to both relative motion in the atmosphere and changes in its mass distribution. Previous studies have shown that AAM is the primary source of subdecadal variations in the Earth rotation rate [*Eubanks et al.*, 1985; *Chao*, 1989; *Dickey et al.*, 2010], and generally a strong source of polar motion [*Salstein and Rosen*, 1989; *Celaya et al.*, 1999; *Gross et al.*, 2003; *Dobslaw et al.*, 2010].

[4] ERP variations therefore represent, to the extent that other excitation sources can be accounted for or neglected, integral measures of atmospheric variability. This makes them a unique source of information about the atmosphere, which may be used to constrain atmospheric models. The feasibility of this constraint is explored in the present paper.

[5] Earth rotation rate changes are typically quantified as anomalies in the length of a day, or $\Delta$LOD. The mechanism by which atmospheric zonal wind excites $\Delta$LOD is easy to understand: Positive westerly wind anomalies increase the relative axial angular momentum of the atmosphere, which in turn reduces the Earth's rotation rate, causing a positive $\Delta$LOD anomaly (and vice versa).

[6] The atmosphere is the main source of subseasonal variations in $\Delta$LOD [*Dickey et al.*, 1991; *Gross et al.*, 2003], which have been tied primarily to the Madden-Julian oscillation (MJO) in tropical zonal winds, and to the interaction of flow with topography in the Northern Hemisphere [*Anderson and Rosen*, 1983; *Dickey et al.*, 1991; *Rosen et al.*, 1991]. $\Delta$LOD also exhibits strong annual and semi-annual

[1]GFZ German Research Centre for Geosciences, Potsdam, Germany.
[2]Helmholtz-Zentrum für Ozeanforschung Kiel, Kiel, Germany.
[3]Institut für Meteorologie, Freie Universität Berlin, Berlin, Germany.


0148-0227/12/2011JD016555

cycles, due to the asymmetry in the landmass between the Northern and Southern Hemispheres, and the consequent seasonal differences in Northern and Southern Hemisphere jets [*Rosen and Salstein*, 1983; *Rosen et al.*, 1991; *Zhao and Qu*, 1995; *Gross et al.*, 2003; *Dobslaw et al.*, 2010]. Interannual ΔLOD variations have been connected to the El Niño / Southern Oscillation (ENSO) [*Salstein and Rosen*, 1986; *Rosen and Salstein*, 2000; *Dickey et al.*, 2007] and the Quasi-Biennial Oscillation (QBO) in the stratosphere [*Chao*, 1989; *Yu et al.*, 1999], the effects having a roughly 2-to-1 ratio to one another [*Chao*, 1989]. *Rosen and Salstein* [2000] showed that changes in the frequency of ENSO events can be linked to long-term changes in the variability of AAM, which could make such changes observable in the form of ΔLOD. However, on decadal timescales the exchange of angular momentum between the core and mantle of the Earth begins to dominate the forcing of Earth rotation, which makes the degree of atmospheric forcing difficult to identify [*Jochmann and Greiner-Mai*, 1996; *Greiner-Mai and Jochmann*, 1998].

[7] Polar motion is excited by the two equatorial components of AAM, but the relationship is more complicated. Atmospheric excitation comprises about 45% of subseasonal polar motion excitation, with the angular momenta of the ocean and continental hydrosphere making up most of the rest [*Salstein and Rosen*, 1989; *Gross et al.*, 2003; *Bizouard and Seoane*, 2010; *Le Mouël et al.*, 2010]. Interannual polar motion variations have been shown to be primarily due to oceanic mass redistribution [*Gross et al.*, 2003], and have thus been more difficult to connect to specific atmospheric phenomena.

[8] Atmospheric dynamics thus comprise a major component of Earth rotation variations; the ERP-AAM relationship can potentially be used to constrain atmospheric models. *Hide et al.* [1997], for example, showed how comparing the axial AAM of different climate models reveals biases in their zonal wind fields. That study moreover showed that, in modeling axial AAM, agreement between models on one timescale is generally independent of the models' agreement on other timescales.

[9] This study explores the information contained about the atmosphere in ERP observations. Our approach is to compare the atmospheric ERP excitation estimated from (1) geodetic monitoring data, (2) the output of a model constrained by meteorological observations (i.e., atmospheric reanalysis data), and (3) a set of climate model simulations that are unconstrained by meteorological data, but are constrained by boundary conditions and slight nudging of tropical winds to capture the QBO. We shall see below that having time-dependent ocean boundary conditions has a considerable impact on the ability of an atmosphere model to capture interannual variations in Earth rotation excitation, while the presence of QBO nudging has a smaller, but still significant, effect. Comparison of geodetically-observed ERP data and the atmospheric reanalyses shows where closure of the angular momentum budget has been achieved or is still lacking. Comparison of the reanalysis data and free-running simulations shows the potential for gaining information when the modeled atmospheric state is constrained by observations.

[10] The paper is organized as follows. Section 2 explains the ERP observational data used, the model simulations from which geophysical excitation functions are computed, and the atmospheric excitation functions inferred from both sources. Section 3 compares the excitation functions implied by observations to those derived from the reanalyses and atmospheric model simulations, and identifies the key differences between them. Section 4 examines the spatial relationship between a modeled state and its implied ERP excitations. Section 5 summarizes the results and discusses the implications for the future assimilation of ERP observations.

## 2. Models and Observations

[11] The observed ERPs imply a net excitation due to the exchange of angular momentum between the solid Earth, the atmosphere, the ocean, the continental hydrosphere, and core-mantle interaction. We estimate the atmospheric component of this total excitation by subtracting estimates of the excitation due to the ocean, continental hydrosphere, and (for decadal and longer timescales) core-mantle coupling. The resulting residual excitation is then compared to the geophysical atmosphere excitation, estimated from two sources: (1) the ECMWF atmospheric reanalyses, ERA-40 and ERA-Interim, which are constrained by meteorological data, and (2) simulations of the atmosphere model ECHAM5/MESSy, under a range of horizontal and vertical resolutions and with/without time-dependent boundary conditions. The reanalyses, climate model simulations, and observations are described in detail below.

### 2.1. Observed Earth Rotation Parameters

[12] The ERP observations consist of two vector components that define polar motion, and anomalies in the length-of-day. Polar motion is reported in terms of two vector components, $p_1$ and $p_2$, which give the location of the celestial ephemeris pole of the Earth [*Gross*, 1992], typically in units of milli seconds of arc (mas). Length-of-day anomalies, are determined by the difference between the astronomically-measured universal time (UT1), and the international atomic time (French, Temps Atomique International; TAI); ΔLOD is then given by [*Eubanks et al.*, 1985]

$$\Delta\mathrm{LOD} = -\mathrm{LOD}_0 \frac{d(\mathrm{UT1} - \mathrm{IAT})}{d\mathrm{IAT}} \tag{1}$$

where $\mathrm{LOD}_0$ denotes the length of sidereal day, $86160 \times 10^3$ ms.

[13] The ERP data are published online by the International Earth Rotation and Reference Systems Service (IERS) Web site, (http://hpiers.obspm.fr/eop-pc/). Here we have used the EOP-CO4 series from 1962 to 2010. This data set is a composite of observations made by optical astrometry, lunar and satellite laser ranging, Very Long Baseline Interferometry, and GPS. Zonal solid Earth tides affect observed ΔLOD on periods ranging from 5.64 days to 18.6 years, but have been modeled and removed during the EOP-C04 processing. The daily resolution of these data means that semidiurnal and diurnal ocean tide signals are also excluded. Longer ocean tide signals (e.g., 13.6-day tides) remain in the data, but are not relevant to this study since we focus on variations longer than 30 days only.

[14] The ERPs can be related to Earth angular momentum by assuming small perturbations in the Earth's three-

dimensional rotation vector, $\boldsymbol{\omega} = (m_1, m_2, 1 + m_3)\Omega$. These perturbations are related to corresponding perturbations in angular momentum via the linearized Euler equations [*Barnes et al.*, 1983].

$$\mathbf{m}_{\mathrm{eq}} + \frac{i}{\sigma_0}\frac{d}{dt}\mathbf{m}_{\mathrm{eq}} = \boldsymbol{\chi}_{\mathrm{eq}} - \frac{i}{\Omega}\frac{d}{dt}\boldsymbol{\chi}_{\mathrm{eq}} \tag{2}$$

$$\frac{d}{dt}m_3 = \frac{d}{dt}\chi_3. \tag{3}$$

Here $\mathbf{m}_{\mathrm{eq}} \equiv m_1(t) + im_2(t)$ represent the complex-valued perturbation to the orientation of the rotational pole. The $\boldsymbol{\chi}_{\mathrm{eq}} \equiv \chi_1 + i\chi_2$ and $\chi_3$ are corresponding dimensionless excitation functions, defined in the equatorial plane ($\boldsymbol{\chi}_{\mathrm{eq}}$) and axially ($\chi_3$). $\sigma_0$ represents the Chandler frequency of 1/433 days.

[15] The quantities in (2)–(3) are defined in a reference frame that is fixed to and rotating with the Earth. *Gross* [1992] showed that the reported polar motion vector $\mathbf{p}_{\mathrm{eq}} \equiv p_1 - ip_2$ can be related to $\mathbf{m}_{\mathrm{eq}}$

$$\mathbf{m}_{\mathrm{eq}} = \mathbf{p}_{\mathrm{eq}} - \frac{i}{\Omega}\frac{d}{dt}\mathbf{p}_{\mathrm{eq}}, \tag{4}$$

which results in the following form of (2):

$$\mathbf{p}_{\mathrm{eq}} + \frac{i}{\sigma_0}\frac{d}{dt}\mathbf{p}_{\mathrm{eq}} = \boldsymbol{\chi}_{\mathrm{eq}}. \tag{5}$$

Equation (5) relates the observed polar motion vectors $p_1$ and $p_2$ to the angular momentum excitation functions $\chi_1$ and $\chi_2$, to be described in the next section.

[16] Equation (3) relates observed changes in the rate of Earth rotation to an axial excitation function $\chi_3$. The solution to (3) is simply $m_3 = \chi_3 + C$, where $C$ is an arbitrary constant. Note that

$$m_3 = \frac{\omega_3 - \Omega}{\Omega} = -\frac{\Delta\mathrm{LOD}}{\mathrm{LOD}_0}, \tag{6}$$

where $\Omega = 7.292115 \times 10^{-5}$ rad/s is the mean Earth angular velocity and $\mathrm{LOD}_0 = 2\pi/\Omega = 86164$s represents the length of a sidereal day. Thus negative changes in the axial excitation function $\chi_3$ (i.e., negative excitation of the Earth's angular momentum) denote positive anomalies in the length-of-day, $\Delta$LOD.

### 2.2. Geophysical Atmospheric Excitation Functions

[17] The atmospheric component of the excitation functions defined above, or atmospheric excitation functions (AEFs), have been derived in detail by *Barnes et al.* [1983], though the parameters quantifying the elastic deformation of the Earth have subsequently been revised several times. Here we adopt the deformation parameters given by *Gross* [2009], but note that adequate values of these factors are still under discussion [e.g., *Chen and Shen*, 2010]. Each AEF consists of a term that reflects changes in the inertia tensor (hereafter the "mass term"), and term that reflects changes in the relative angular momentum (hereafter the "wind term"). The equatorial AEFs, which excite variations in $p_1$ and $p_2$, have combined mass and wind terms

$$\chi_1^{\mathrm{M}} + i\chi_2^{\mathrm{M}} = \frac{-1.098R^4}{(C-A)g}\int_0^{2\pi}\int_{-\pi/2}^{\pi/2} p_s \sin\phi\cos^2\phi e^{i\lambda}\mathrm{d}\lambda\mathrm{d}\phi \tag{7}$$

$$\chi_1^{\mathrm{W}} + i\chi_2^{\mathrm{W}} = \frac{-1.5913R^3}{\Omega(C-A)g}\int_{p_s}^{p_{\mathrm{top}}}\int_0^{2\pi}\int_{-\pi/2}^{\pi/2} (u\sin\phi + iv)\cos\phi e^{i\lambda}\mathrm{d}\lambda\mathrm{d}\phi\mathrm{d}p, \tag{8}$$

where the superscripts W and M denote the wind and mass terms, respectively. Here $R$ is the radius of the Earth and $C = 8.0365 \times 10^{37}$ kgm$^2$ and $A = 8.0101 \times 10^{37}$ kgm$^2$ represent, respectively, the axial and next-largest principal moments of inertia of the whole Earth [*Gross*, 2009]. The $\chi_1$ and $\chi_2$ are defined in radians, but will be compared here in terms of milli arcseconds (mas).

[18] The axial AEF, which excites $\Delta$LOD, has mass and wind terms

$$\chi_3^{\mathrm{M}} = \frac{0.748R^4}{C_m g}\int_0^{2\pi}\int_{-\pi/2}^{\pi/2} p_s\cos^3\phi\mathrm{d}\lambda\mathrm{d}\phi \tag{9}$$

$$\chi_3^{\mathrm{W}} = \frac{0.997R^3}{C_m\Omega g}\int_{p_s}^{p_{\mathrm{top}}}\int_0^{2\pi}\int_{-\pi/2}^{\pi/2} u\cos^2\phi\mathrm{d}\lambda\mathrm{d}\phi\mathrm{d}p, \tag{10}$$

where $C_m = 7.1236 \times 10^{37}$ kgm$^2$ denotes the principal moment of inertia of the mantle. These functions are dimensionless, and can be related to equivalent $\Delta$LOD using equation (6).

[19] Note that in (8) and (10) the winds are integrated over pressure, to the pressure at the top of the modeled atmosphere, here represented by $p_{\mathrm{top}}$. In the present study, $p_{\mathrm{top}}$ will be either at 0.1 hPa, for reanalysis data, or at 0.01 hPa, for climate model simulations performed specifically within this study. Both model tops include the stratosphere, and we do not expect the higher atmospheric levels to make a significant impact on the resulting atmospheric excitation.

[20] In computing (7)–(10) we additionally make the so-called inverse barometer (IB) [*Wunsch and Stammer*, 1997] approximation, meaning that we assume that the ocean responds instantaneously to changes in surface pressure with a corresponding change in sea level. Practically, this means that we average the surface pressure over all grid boxes with zero land fraction, and assume the resulting average surface pressure to be the same value over all sea-grid boxes.

[21] The following two sections describe the application of the excitation functions, derived above, to both atmospheric reanalyses and model simulations that are unconstrained by meteorological data but do have certain boundary forcings. All data sources are summarized in Table 1, which describes the available range of each data set, its resolution and model top, along with the type of observational constraint applied in each case (to be described below).

### 2.3. ECMWF Reanalysis Data

[22] Geophysical AEFs have been calculated by *Dobslaw et al.* [2010] from two European Centre for Medium-Range Weather Forecasts (ECMWF) reanalysis sets, ERA-40 [*Uppala et al.*, 2005], and ERA-Interim [*Uppala et al.*,

**Table 1.** Summary of Excitation Function Sources Considered in This Study

| Data Set | Period | Resolution | Model Top | Observational Constraint[a] |
|---|---|---|---|---|
| EMAC31[b] | 1958–2000 | T31L39 | 0.01 hPa | QBO |
| EMAC42[b] | 1958–2000 | T42L39 | 0.01 hPa | QBO |
| EMAC63[b] | 1958–2000 | T63L39 | 0.01 hPa | QBO |
| CCMVal[c] | 1960–2000 | T42L90 | 0.01 hPa | QBO, BCs |
| ERA-40[d] | 1958–2001 | T159L23 | 0.1 hPa | Full DA |
| ERA-Interim[e] | 1989–2008 | T255L39 | 0.1 hPa | Full DA |
| OAM-40[f] | 1958–2001 | | | ERA-40 BC |
| HAM-40[f] | 1958–2001 | | | ERA-40 BC |

[a]Here "QBO" denotes nudging of tropical stratospheric winds to force a QBO. "BCs" denotes the use of realistic (observed) boundary conditions. "Full DA" indicates assimilation of the full suite of available meteorological observations.
[b]Original simulations performed for this study.
[c]Simulation performed for the CCMVal Project [*Morgenstern et al.*, 2010; *SPARC CCMVal*, 2010].
[d]*Uppala et al.* [2005].
[e]*Uppala et al.* [2008].
[f]Simulations performed by *Dobslaw et al.* [2010] using the OMCT and LSDM models for OAM and HAM, respectively, with ERA-40 boundary forcing.

2008]. An atmospheric reanalysis is the product of a long-term assimilation of meteorological data into a state-of-the-art model, and represents the best possible estimate of the atmospheric state over a period of time, given the best models and most complete observations available.

[23] The ERA-40 data set covers the period from September 1958 to August 2002, and is constrained by meteorological and oceanic data including wind, temperature, specific humidity, and surface pressure from ground-based methods (e.g., radiosondes, balloons, and surface stations), with the addition of observations from aircraft and satellites in the mid and late seventies, including ozone observations in the late seventies, and starting in the 1980s and 90s, water vapor and oceanic wave height. The observations are assimilated using 3D-Variational Assimilation (3D-Var) [*Uppala et al.*, 2005]. The ERA-40 data have $1.25° \times 1.25°$ horizontal resolution (T159 spectrally), on 23 pressure levels reaching up to 0.1 hPa. Here we use only the data that overlap with both the available ERP observations and the atmospheric model simulations (next section), namely 1962–2000.

[24] ERA-Interim is a continuously-updated reanalysis starting at the year 1989, with subsequent updating until the next major reanalysis release. The major differences to ERA-40 are the assimilation method used (ERA-Interim employs 4D-Var, which includes the propagation of uncertainty statistics backward and forward in time), model resolution, improved formulation of background error statistics, improved model physics, and improved observation handling. The ERA-Interim data have $1° \times 1°$ horizontal resolution (T255 spectrally), on 37 pressure levels reaching up to 0.1 hPa [*Uppala et al.*, 2008].

[25] The AEFs computed from the ERA-40 and ERA-Interim data have been provided by H. Dobslaw and are similar to those presented by *Dobslaw et al.* [2010]. Because the period of overlap between ERA-Interim data and the atmospheric simulations (next section) is quite short (1989–2000), all computations for ERA-Interim data will be performed over the period of overlap between it and the available ERP data, namely 1989–2008.

### 2.4. Climate Model: ECHAM5/MESSy (EMAC-FUB)

[26] Atmospheric simulations without data assimilation are performed using the ECHAM5/MESSy Atmospheric Chemistry model [*Jöckel et al.*, 2006] with the Free University of Berlin (FUB) radiation scheme [*Nissen et al.*, 2007], hereafter referred to as EMAC-FUB. EMAC-FUB consists of the Modular Earth Submodel System (MESSy), built around the ECHAM5 global circulation model. The model uses terrain-following pressure-hybrid vertical coordinates. Gravity waves are simulated using the *Hines* [1997] parametrization scheme [*Manzini and McFarlane*, 1998], and a "sponge" layer of increased diffusion at the model top prevents artificial reflection of waves.

[27] The modular structure of EMAC-FUB includes the options of running with or without (stratospheric and tropospheric) chemistry [*Sander et al.*, 2005], simulating a QBO by nudging of stratospheric winds, and with constant or time-varying boundary conditions (SSTs, sea ice extent, solar cycle, volcanic aerosols, and GHG and ODS (ozone depleting substances) emissions). Four EMAC-FUB simulations are considered here; three are dynamics-only runs with climatological boundary conditions, and one is a full-chemistry run with realistic boundary conditions, performed prior to this study within the SPARC Chemistry-Climate Model Validation (CCMVal) initiative [*SPARC CCMVal*, 2010; *Morgenstern et al.*, 2010]. All four runs include nudging of stratospheric winds to simulate a QBO (described below). The simulations, their respective data periods, resolution, and observational constraints, are summarized in Table 1.

#### 2.4.1. CCMVal Climate Simulation

[28] Data from the CCMVal-REFB1 experiment were available for the period from 1960 to 2000, and includes full interactive chemistry, and is constrained by observed SST, sea ice, solar cycle, volcano, and GHG and ODS emission boundary conditions. The horizontal resolution is T42, with the model top at 0.01 hPa (~83 km) and L90 vertical resolution. The high vertical resolution enables a self-simulated QBO [*SPARC CCMVal*, 2010], which is only nudged slightly toward observed winds in order to attain the correct QBO phase [*Giorgetta et al.*, 2006]. Only the period of overlap with the ERP data (1962–2000) is considered here.

#### 2.4.2. Simulations With Climatological Boundary Conditions

[29] Three dynamics-only EMAC-FUB simulations were performed specifically within this study. These runs have no interactive chemistry, and represent time-slice experiments in the sense that GHG are kept constant at year-2000 levels, sea surface temperatures (SSTs) and sea ice extent at their 1960 to 2000 climatological monthly values, and the solar activity for the year 2000 is repeated for all years. Only one time-varying factor is kept in these runs, namely that the QBO is simulated by nudging tropical stratospheric winds toward observations. This was done in order to more accurately represent the internal variability of the atmosphere and, as we shall see in section 3, to show the extent to which simulation of the QBO affects a model's simulation of Earth rotation variations.

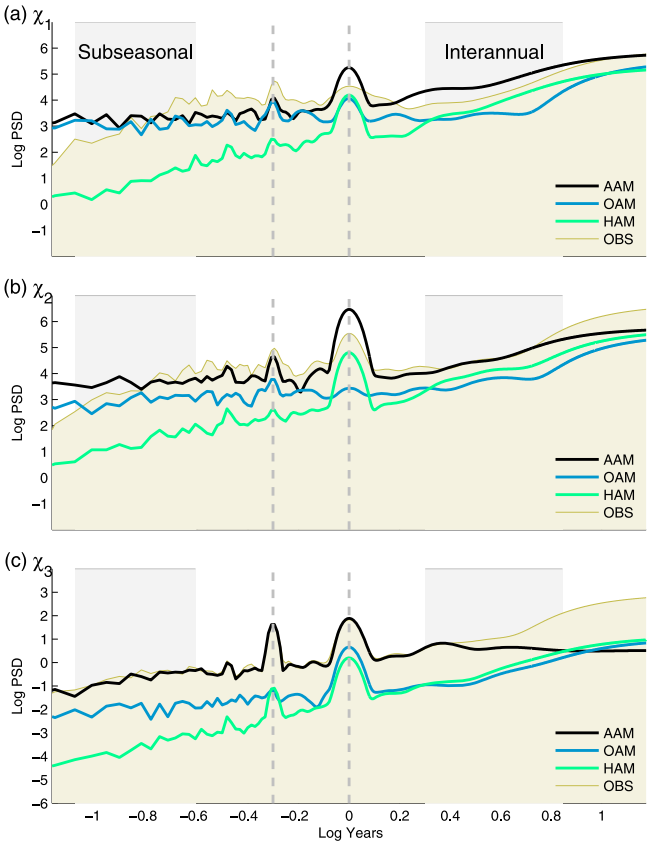


**Figure 1.** Power spectra of observed polar motion vectors (a) $p_1$ and (b) $p_2$, and (c) length-of-day $\Delta$LOD changes, compared to the corresponding spectra of excitations from AAM, OAM, and HAM, estimated from data described in Table 1. The gray shaded bars and dashed lines indicate the frequency bands (subseasonal, semiannual, annual, and interannual) on which the majority of this study focuses.

[30] These simulations differ only in horizontal resolution, and are abbreviated accordingly: Simulation EMAC31 is run at spectral horizontal resolution T31 (3.75° × 3.75°), EMAC42 at T42 (2.8° × 2.8°), and EMAC63 at T63 (1.8° × 1.8°). All three simulations have 39 vertical levels, extending to 0.01 hPa. The simulations are run from 1958 to 2000, effectively discarding the first four years since only the years 1962–2000 overlap with the ERP observations (section 2.1).

### 2.5. Geodetically-Inferred Atmospheric Excitation Functions

[31] In order to compare the geophysical AEFs estimated from the above data sets to the observed ERPs, we must subtract estimates of the excitation due to ocean, continental hydrosphere, and core-mantle angular momenta (OAM, HAM, and CAM, respectively) from the observations.

[32] Two residual AEFs are computed in order to obtain an estimate of the uncertainty in the residual estimation. In the first, OAM and HAM estimates made by *Dobslaw et al.* [2010] from simulations of the Ocean Model for Circulation and Tides (OMCT) [*Thomas et al.*, 2001; *Thomas*, 2002] and the Land Surface and Discharge Model (LSDM) [*Dill*, 2009] are used. These simulations cover the same period as the AEFs computed from ERA-40, and use that data set as a boundary condition. In the second estimate, OAM excitations computed from the ECCO model [*Gross et al.*, 2005], which are available online (IERS Earth Orientation Data, 2009, ftp://ftp.iers.org/), are substituted for the OMCT OAM estimates.

[33] An estimate of Earth rotation excitation by CAM is only applied when examining periods longer than 7 years. Here we use excitation functions generated from preliminary runs of the geomagnetic field model C3FM2 [*Wardinski and Holme*, 2006].

[34] By subtracting these estimates from the total excitation implied by the observations, we attain an estimate of the atmospheric component. We will refer to this component as the observed residual AEF. Note also that $\chi_1$ and $\chi_2$, naturally expressed in radians, can be easily converted to milliarcseconds (mas) in order to relate them to observed polar motion angles $p_1$ and $p_2$, while $\chi_3$ can be mapped to equivalent $\Delta$LOD using (6).

## 3. Results: Observed Versus Modeled Atmospheric Excitation

[35] The ERA-40 and -Interim data sets constitute a best-possible estimate of the atmospheric state over the period considered in this study. Comparison between the AEFs in the reanalyses and the observed ERPs therefore gives an estimate of the strength of atmospheric excitation of $\Delta$LOD and PM. Comparison between the reanalyses and the EMAC-FUB simulations then shows where assimilation of meteorological data improves modeled Earth rotation variations, and where other constraints (in our case, time-dependent boundary conditions and QBO nudging) are sufficient. With this framework in mind, we begin with a spectral comparison of the excitation functions implied by observations, the reanalyses, and the EMAC-FUB simulations, and then compare the relevant timescales separately.

### 3.1. Spectral Comparison

[36] Figure 1 shows power spectral densities (PSDs) of the three observed ERPs and their corresponding AEFs estimated from the ERA-40 data, as well as the excitation functions of OAM and HAM, as described in section 2.5 and Table 1. The spectra are computed using Goertzel's algorithm [*Proakis and Manolakis*, 1996] to compute the power spectral density at frequencies ranging from 5 days to 15 years, in 5 day increments. Specific timescales on which we will focus in this paper are emphasized by shading and dashed lines: subseasonal variations (30–90 days), the annual and semiannual peaks, interannual variations (2–7 years), and long-term variations (7+ years).

[37] In all three cases it can be seen that the atmospheric contribution to each observed ERP depends strongly on timescale. For the polar motion excitations ($\chi_1$ and $\chi_2$) (Figures 1a and 1b), atmospheric excitation is generally the strongest source, though the atmospheric excitation actually exceeds the power of the observed polar motion at timescales shorter than about 60 days (a result that was also found by *Nastula et al.* [2009]), at the annual peak, and longer than about a year, especially in $\chi_1$. However, excitation by OAM is comparable to that of AAM at the shortest timescales, while HAM excitation gains power at the longest timescales, which might potentially balance the angular momentum budget at each timescale. For the annual peak,

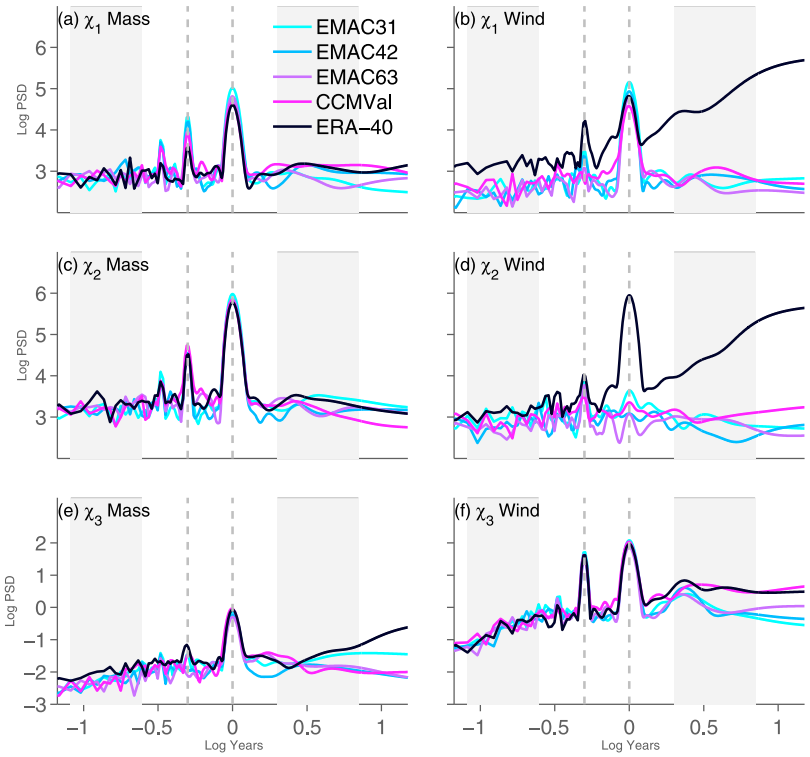


**Figure 2.** Comparison of the modeled AAM excitations due to (a, c, e) mass redistribution and (b, d, f) wind, with rows showing the three different AEF components. Each panel compares the four data-unconstrained EMAC simulations to the data-constrained ERA-40 data set.

*Dobslaw et al.* [2010] show that adding the OAM excitation to that of AAM improves the angular momentum balance, though complete closure of the angular momentum budget in this frequency range has not yet been achieved.

[38] In contrast to polar motion, ΔLOD excitation (Figure 1c) is strongly dominated by the atmosphere at all timescales shorter than about 3 years, with OAM and HAM excitations about two orders of magnitude smaller. The relative magnitude of AAM excitation of ΔLOD diminishes at timescales longer than about three years; here other excitations, especially core-mantle effects, become important. These will be discussed in section 3.5.

[39] Figure 2 examines how the various constrained and unconstrained models presented in section 2.4 capture AAM on the range of timescales shown in Figure 1. Each panel in Figure 2 spectrally compares the three AEFs estimated from ERA-40 to those estimated from the four EMAC-FUB simulations described in section 2.4. Here the spectra are split further into their contributions from changing mass distribution (Figures 2a, 2c, and 2e) and wind (Figures 2b, 2d, and 2f).

[40] The most clear differences between the ERA-40 and the EMAC-FUB excitations are seen in the wind terms of each excitation component (Figures 2b, 2d, and 2f). For the polar motion excitation functions $\chi_1$ and $\chi_2$, the ERA-40 data show much more power at all frequencies, but especially at interannual and longer timescales. Since the equatorial AAM excitation in ERA-40 does seem to roughly match the excitation power of the polar motion observations on this timescale (Figures 1a and 1b), this suggests that all four EMAC-FUB runs are missing a key feature of interannual variability. This is of course not surprising for the climatological EMAC simulations (EMAC31-EMAC63), but even the CCMVal simulation, which has realistic boundary conditions, does not seem to contain enough interannual polar motion excitation. We have also found, however, that the magnitude of interannual variations decreases in both the observed polar motion and the ERA-40 AAM excitation, from about 1980 onward (this will be discussed further in section 3.4).

[41] The peaks at the annual cycle and its subharmonics show little variation between the different model runs, except in the wind term of $\chi_2$ and both terms of $\chi_1$. In $\chi_1$ especially there appears to be convergence to the ERA-40 peaks with increasing model resolution. This will be investigated in more detail in section 3.3.

[42] Finally, the clearest difference between the CCMVal simulation, which has dynamic boundary conditions, and the EMAC-FUB simulations with climatological boundary conditions and only QBO forcing, is in interannual to long-term variations of $\chi_3$ (Figure 2f). Figures 2e and 2f compare the excitation spectra of the mass (Figure 2e) and wind (Figure 2f) terms of $\chi_3$. It can be seen that the EMAC-FUB simulations generally simulate the same power of ΔLOD excitation as the ERA-40 data for annual and shorter variations. For interannual and longer variations, the ERA-40 data and the CCMVal simulation have about an order of magnitude greater power than the simulations with climatological boundary conditions. This indicates that, as found by *Rosen and Salstein* [2000], SST variability, which is one of

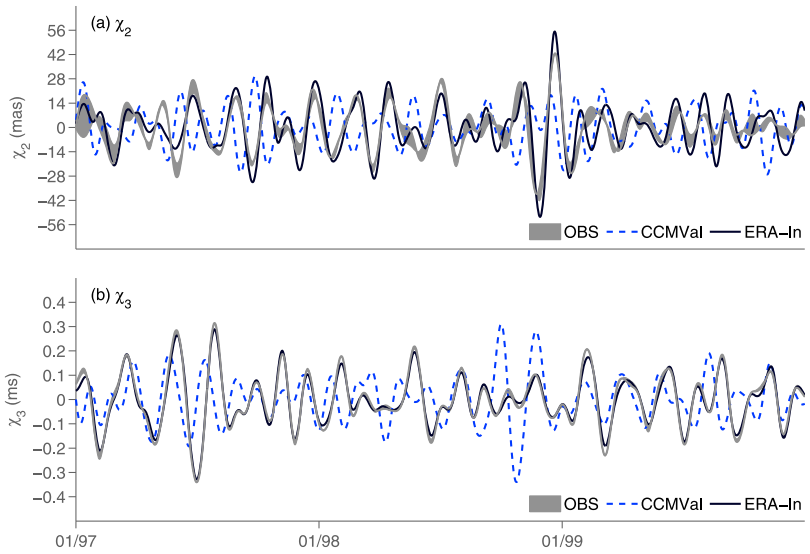


**Figure 3.** Time series of the geophysical AEFs (a) $\chi_2$ and (b) $\chi_3$, estimated from the ERA-Interim data set and the CCMVal simulation. The geodetic residual AEFs (OBS) are estimated as described in section 2.5, with the difference between the two estimates shaded. Here all time series are digitally band-pass filtered to isolate variations with periods between 30 and 90 days.

the dynamic boundary conditions in the CCMVal simulation, has a strong influence on interannual variations in axial AAM. This will be discussed in more detail in section 3.4.

[43] In the following sections, the AEFs produced by the ERA reanalysis sets, and the EMAC-FUB simulations, will be examined more closely by frequency band.

### 3.2. Subseasonal Variations (30–90 Days)

[44] We focus first on the 30–90 day subseasonal band. Figure 3 shows sample time series of $\chi_2$ and $\chi_3$ over the period 1997–1999, comparing the geophysical AEFs from the CCMVal simulation and ERA-Interim, to the residual AEFs estimated by subtracting OAM and HAM estimates from the observations (section 2.5). The AEFs computed from ERA-Interim data are nearly identical to those from ERA-40 over this time span; hence the ERA-40 data are omitted from this plot for clarity. Here all time series are filtered using a second-order Butterworth band-pass filter to isolate 30–90 day periods. The time series for $\chi_1$ are comparable to those for $\chi_2$ and are therefore omitted. In the $\chi_3$ time series (Figure 3b), the fluctuations largely reflect the 40–60 day MJO [*Anderson and Rosen*, 1983]. The difference between the two estimates of the residual AEF is shaded, though this difference is often quite small.

[45] Two things can immediately be seen. First, whereas the ERA-40/ERA-Interim AEFs closely follow the observed residuals in both panels, the AEFs estimated by EMAC-FUB do not. This is to be expected, since the CCMVal simulation is not constrained by meteorological data, and subseasonal AEF variations reflect nonspecific, synoptic weather activity that can't be expected to have a significant correlation to the ERP observations on this timescale. Second, the disagreement between ERA-40/ERA-Interim and the observed residual AEF is much larger in $\chi_2$ than in $\chi_3$, as is the estimated uncertainty in the residual itself. Thus it can be seen that the axial component of AAM excitation on subseasonal excitations is generally easier to estimate than the equatorial components, but both can be captured better when the atmosphere model is constrained by meteorological data.

[46] Figure 4 shows the correlations between the observed ERPs and all the available AEF estimates (Table 1), as well as the OAM and HAM excitations (Table 1). The correlations are computed over the period 1962–2000 (except for ERA-Interim, where the correlation is computed over the period 1989–2008), after all time series are band-pass filtered to isolate 30–90 day periods. Since the filtered time series all have some serial correlation and are generally not normally distributed, the correlations are computed using a 1000 -member nonparametric stationary bootstrap algorithm [*Mudelsee*, 2003]. The bootstrap method also yields an estimate of the 95% confidence interval of each correlation estimate, which is shown in the plot by error bars.

[47] As mentioned above, one would not expect the EMAC-FUB simulations to have a significant correlation to the observations at this timescale, since they reflect arbitrary years. Indeed, the correlations estimated for the four EMAC-FUB simulations are all found to be statistically indistinguishable from zero, with the exception of $\chi_2$ in EMAC63, where variations are very marginally correlated with observations. Note also that the time-varying boundary forcing in the CCMVal simulation also shows no significant correlations to the observations, implying that the atmospheric mechanisms that cause subseasonal ERP variations cannot be captured when time-dependent boundary conditions are given.

[48] In contrast, the data-constrained AEF estimates from ERA-40 and ERA-Interim have significant nonzero correlations in all three vector components, ERA-Interim showing the highest correlation to observations (reflecting the improved data of this reanalysis). It can clearly be seen that the amount of observational variance explained by atmospheric excitation is close to 1.0 for $\chi_3$, which reflects how strongly the atmosphere dominates $\Delta$LOD variations on this timescale (compare Figure 1c, which shows that the OAM and HAM

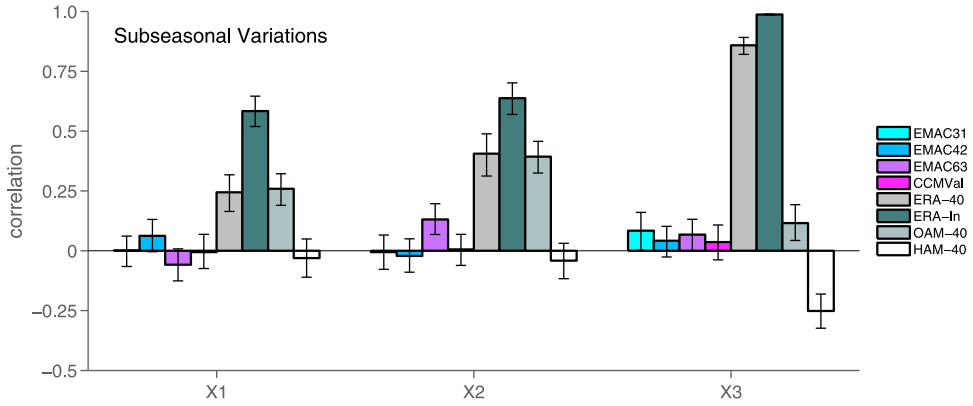


**Figure 4.** Correlations between the observed ERPs ($p_1$, $p_2$, and $\Delta$LOD) and their corresponding excitation functions ($\chi_1$, $\chi_2$, and $\chi_3$, respectively) estimated by the different data sets described in Table 1. Correlations are estimated using a 1000-sample bootstrap algorithm, the mean of which is indicated by the colored bars, with the error brackets indicating the 95% certainty interval.

excitations at this timescale are several orders of magnitude smaller.). However, oceanic excitation (OAM-40) is found to be significant for all three components, especially the equatorial ones, and axial ($\chi_3$) excitation from the continental hydrosphere (HAM-40) also shows a weak but significant anticorrelation to the observations. This is not really surprising, since the boundary fluxes (precipitation, evaporation, and temperature) in both the ocean and continental hydrosphere models come from ERA-40 [*Dobslaw et al.*, 2010]. Figure 4 suggests that subseasonal $\Delta$LOD excitation by the atmosphere tends to coincide with opposite excitation by the continental hydrosphere.

[49] Figure 4 shows that constraining a model with meteorological observations improves the fit to observed ERPs in all three components. This in turn suggests that there may be potential for using ERP data to additionally constrain models. It could be that ERP observations can be used to inform an atmospheric model similarly to meteorological observations, as a constraint on the global state, though this remains to be tested. However, OAM and HAM excitation cannot easily be neglected on this timescale, and may even (in the case of HAM excitation of $\chi_3$) cancel out some of the atmospheric excitation.

[50] These excitation sources should be carefully accounted for when comparing an atmospheric model with ERP data. In light of this, we speculate that assimilation of ERPs could also be useful simply as a way to close the budget of geophysical Earth rotation excitation relative to observations, while adjusting each Earth system component in some optimal, physical way.

### 3.3. Annual Cycle

[51] As shown in Figures 1 and 2, the annual variation is a dominant signal in both polar motion and $\Delta$LOD, as well as their corresponding AEFs. The annual variation of the equatorial AEFs, $\chi_1$ and $\chi_2$, can be explained largely in terms of boreal winter high pressure anomalies over Eurasia, which contribute negatively to both $\chi_1$ and $\chi_2$ [*Dobslaw et al.*, 2010]. Similar high-pressure anomalies over Australia and South America during austral winter mostly affect $\chi_2$ (as can be seen by examining the weighting functions for mass; see auxiliary material), but in this case the contributions from the South American and Australian continents largely cancel each other out [*Dobslaw et al.*, 2010].[1] For $\chi_3$, the annual cycle is largely due to seasonality in extratropical jets: the $\cos^2\phi$ weighting for zonal wind means that the angular momenta of zonal jets in the Northern and Southern Hemispheres partially cancel each other, except that the higher landmass in the Northern Hemisphere causes stronger seasonal variation in the jets there. This means that axial AAM is minimal in boreal summer, i.e. there is a minimum in the equivalent $\Delta$LOD (see also auxiliary material).

[52] In Figure 5, the annual and semiannual cycles in the observed ERPs are compared to the AEFs estimated geophysically from the ERA-Interim data. The annual AEFs computed from ERA-40 data are very close to those from the ERA-Interim data, and are therefore omitted from this and Figure 6. Each panel shows the climatological-mean, monthly-mean anomalies of the ERPs and corresponding AEFs from their annual means. The climatological 1-$\sigma$ standard deviation for each case is shown by shading. The $\chi_2$ and $\chi_3$ show strong annual cycles in both observations and the excitations, while $\chi_1$ is more semiannual in nature.

[53] The $\chi_1$ and $\chi_2$ in ERA-Interim also differ noticeably from the observations in both amplitude and phase, while $\chi_3$ estimated from the reanalysis corresponds closely to the $\Delta$LOD observations. This difference can to an extent be explained by OAM and HAM excitation of polar motion. This is examined more closely by *Dobslaw et al.* [2010]; in the present study we will focus on the difference between the various geophysical AEF estimates (Figure 5).

[54] To that end, Figure 6 compares the geophysical AEFs from ERA-Interim to the four EMAC-FUB simulations. As in Figure 5, climatological-mean, monthly-mean anomalies are shown, but now further separating the AEFs into wind and mass contributions. Here the shading shows the standard deviation of year-to-year variability in the ERA-Interim AEFs.

[55] As expected, the annual cycles in the equatorial AEFs are largely dominated by the mass terms, while the annual cycle in $\chi_3$ is dominated strongly by the wind term. The

[1] Auxiliary materials are available in the HTML. doi:10.1029/2011JD016555.

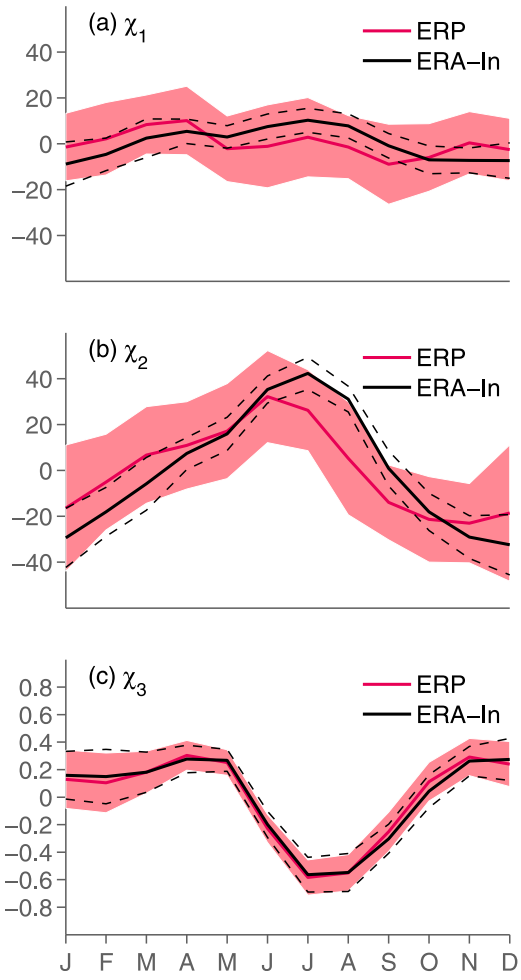


**Figure 5.** Monthly mean values of observed ERPs and their corresponding excitations: (a) $p_1$ ($\chi_1$), (b) $p_2$ ($\chi_2$), and (c) $\Delta$LOD ($\chi_3$). Each panel compares the observed ERPs (red) to the AEFs estimated from ERA-Interim (black). The year-to-year standard deviations for each case are shown by red shading (for the ERPs) and dashed lines (for ERA-Interim).

strongest differences between different data sets is seen in $\chi_1$ (Figure 6b). According to the ERA-40 data, this component has only a weak annual cycle in the mass term (Figure 6a), and almost no annual signal in the wind term (Figure 6b), resulting in a strong semiannual variation in the total (Figure 5a). In contrast, $\chi_1$ in the EMAC-FUB simulations has pronounced maxima (minima) in the wind (mass) terms in boreal summer. There is also an apparent convergence toward the ERA-Interim result as EMAC-FUB resolution is increased.

[56] The annual cycle of $\chi_2$ is dominated by the mass term (Figure 6c) in all five data sets, with almost no annual signal in the wind term (Figure 6d). This dominance of the mass term in the annual cycle of the equatorial AEFs is generally attributed to the fact that annual fluctuations in winds are primarily comprised of differences in zonal jets between the Northern and Southern Hemispheres; since zonal winds in the equatorial weighting functions follow a $\sin\phi\cos\phi$ latitudinal weighting (equation (8)), Northern and Southern Hemisphere jet fluctuations tend to compensate for one another in the global integral [*Dobslaw et al.*, 2010]. However, the longitudinal weighting of zonal wind in $\chi_1$ and $\chi_2$ is such that, in the Northern Hemisphere, $\chi_1$ is more strongly weighted over the oceans, and $\chi_2$ more strongly over continents (see Figure 1 in auxiliary material Text S1). It is shown in the auxiliary material that the EMAC-FUB simulations have much stronger variance in seasonal jets over the North Atlantic, just west of the Greenwich Meridian, coinciding with a local maximum in the $\cos\lambda$ weighting for zonal wind in $\chi_1$ (equation (8)). The reanalyses, presumably because they are constrained by data, have lower variance in the strength of Atlantic jets, and thus a less pronounced seasonal cycle in the wind excitation component of $\chi_1$.

[57] Far less sensitivity to the model used is seen in the annual cycle of $\Delta$LOD (Figures 5c, 6e, and 6f), which is strongly dominated by the wind term (Figure 6f). As in work by *Hide et al.* [1997], even the data-unconstrained models largely agree with reanalyses in the annual cycle of $\chi_3$, much more so than subseasonal variations and (as we shall see in the next section) interannual variations. *Hide et al.* [1997] also found that the annual cycle in $\chi_3$ from free-running models was somewhat lower in amplitude, on average, than the $\chi_3$ produced by a reanalysis; in contrast we find here that the AEFs computed the EMAC-FUB simulations and the ERA reanalyses agree closely, in both amplitude and phase (Figure 5). Moreover, the three EMAC-FUB experiments of different resolutions (Figures 6e and 6f) show very little difference.

[58] Thus, while the annual fluctuation is the most clear signal in all three ERPs, both data-constrained and data-unconstrained models tend to reproduce this fluctuation well in two components, $\chi_2$ and $\chi_3$. Thus there may not be much to be gained in reconciling models to this mode of variation in the ERP observations. Future constraint of atmospheric models by ERP observations is likely to most usefully inform the component of the annual cycle that has the largest prior disagreement with the observations, in this case $\chi_1$, and maybe to some extent $\chi_2$. In this component, reconciliation of model-estimated excitation with observations would mean constraining the amplitude of seasonal zonal jets.

### 3.4. Interannual Variations (2–7 Years)

[59] Figure 7 shows the time series of $\chi_2$ and $\chi_3$, comparing the geophysical AEFs in the ERA-40 data and CCMVal simulation to the geodetic residual AEF inferred from observations, as in Figure 3, but now comparing 2–7 year oscillations for the entire period of overlap, 1962–2000. The ERA-Interim data are omitted from Figure 7 since they only overlap with the last 21 years of the period considered. For $\chi_2$, the interannual fluctuations post-1980 are about a fourth the magnitude of the annual cycle. For $\chi_3$ interannual fluctuations (Figure 7b) are comparable in magnitude to the annual cycle.

[60] The difference between the two estimates of the residual AEF, again shaded, is now much more visible. In $\chi_2$, both the observed residual AEF and the ERA-40 time series show large fluctuations and poor agreement with each other, but agreement increases from the early 1980s onward. This reflects improvements in accuracy in both the geodetic residual (following the implementation of space geodetic observing techniques) and the ERA-40 reanalysis (due to the availability of satellite data for assimilation). ERA-Interim

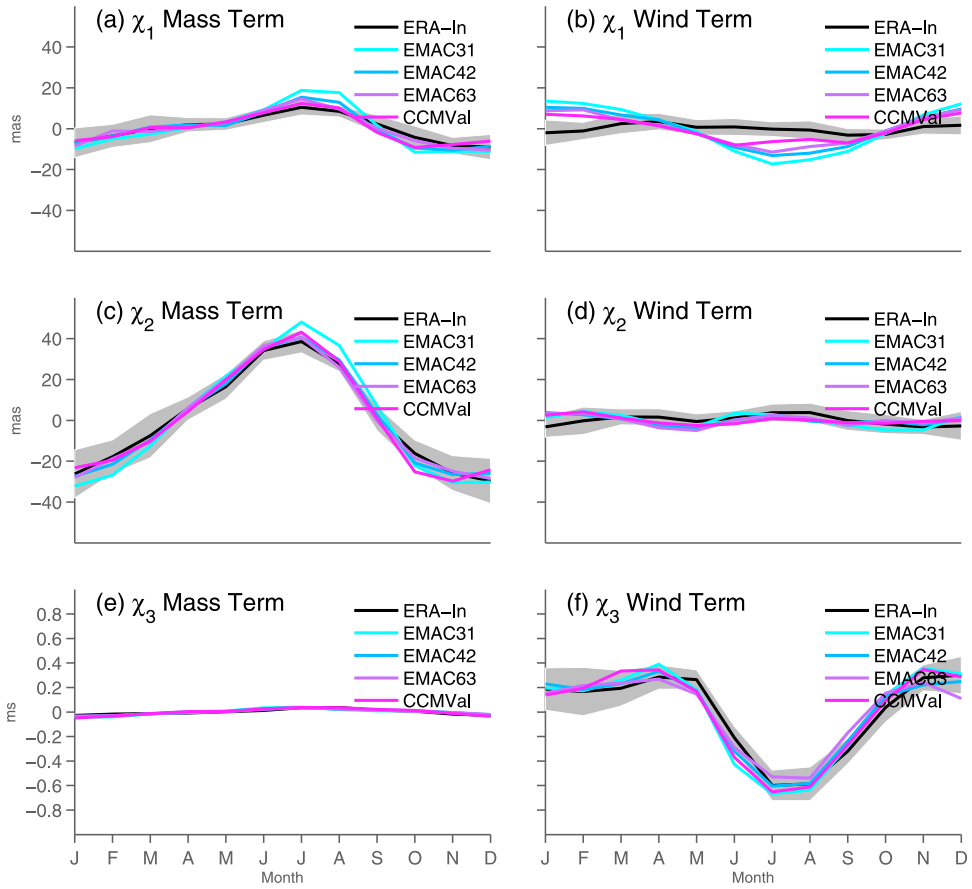


**Figure 6.** Monthly mean values of the three excitation functions, comparing the (a, c, e) mass terms and (b, d, f) wind terms. Each panel compares the four EMAC-FUB simulations to the ERA-Interim data. The year-to-year standard deviation in the ERA-Interim data is shown by gray shading.

data begin in 1989, and because the resulting AEFs are quite close to the AEFs computed from ERA-40 data, they are omitted from Figure 7.

[61] The negative Southern Oscillation Index (SOI) is superimposed on the $\chi_3$ (Figure 7b) time series in order to illustrate the relationship between interannual variations in $\Delta$LOD ($\chi_3$) and ENSO. SOI is related to the normalized difference in monthly-mean surface pressure between Tahiti and Darwin, Australia (positive SOI is associated with large pressure difference between Tahiti and Darwin, indicating cold Pacific SSTs, i.e. La Niña conditions, and vice versa), and thus is a measure of the strength of the atmospheric component of ENSO. The primary effect of El Niño conditions (i.e., negative SOI) on the atmosphere is a weakening of easterly tradewinds in the tropical Pacific (whereas La Niña conditions increase tropical easterlies), which means a strengthening (weakening) of relative AAM, which in turn means a reduction in the angular momentum of the solid Earth, i.e. a positive anomaly in LOD. For example, while the El Niño event in 1997/98 was very strong in terms of the Nino3.4 SST index, its SOI index is considerably smaller than the El Niño event of 1982/83, where the corresponding $\Delta$LOD anomaly is also higher. The relationship between SOI and $\Delta$LOD is not always clear, as seen for example in the very small $\Delta$LOD anomaly during the 1991/1992 El Niño. However, *Chao* [1989] showed that the residual between ENSO-implied axial excitation and observed $\Delta$LOD has a phase and period very close to the axial excitation of QBO winds.

[62] Comparing the interannual $\chi_3$ variations in the CCMVal simulation to ERA-40 and ERA-Interim, it can be seen that, in general, it is difficult to say which agrees better with the geodetic residual $\chi_3$. The effect of the strong El Niño of 1982/83 on $\chi_3$ seems to be underestimated in the CCMVal data, a result which was also found, perhaps coincidentally, by *Hide et al.* [1997] for a variety of other atmosphere models. The CCMVal AEFs now also show some temporal correspondence to observations, since the CCMVal simulation has realistic boundary conditions (i.e., SSTs, sea ice, and the solar cycle) and therefore contains realistic interannual variability. *Hide et al.* [1997] also found that otherwise free-running models with realistic SST boundary conditions (but no QBO forcing) were able to capture the strong 1997/98 El Niño event. Evidently, this relationship is strong enough that having realistic boundary conditions and a realistic QBO produces interannual $\chi_3$ variation that fit the observed residual as well as reanalysis data. This result confirms the findings of *Rosen and Salstein* [2000], who showed that differences in $\chi_3$ interannual variability between a reanalysis set and a model without data assimilation were almost entirely due to differences in the SST boundary conditions.

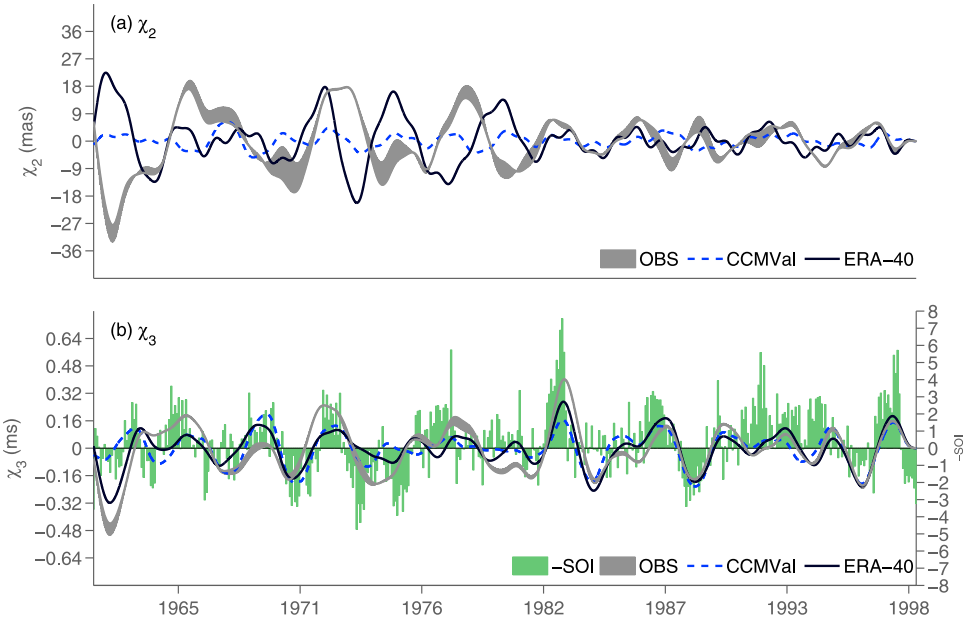


**Figure 7.** Time series of the geophysical AEFs (a) $\chi_2$ and (b) $\chi_3$, estimated from the ERA-40 data set and the CCMVal simulation. The observed residual AEFs are estimated as described in section 2.5, with the difference between the two estimates shaded. Here all time series are digitally band-pass filtered to isolate variations with periods between 2 and 7 years. The green bars indicate the negative Southern Oscillation Index (-SOI).

[63] Correlations between the ERPs and the corresponding geophysical excitation estimates are examined in Figure 8. As in Figure 4, correlations are computed using a 1000 - sample bootstrap estimate, and the 95% confidence interval of each correlation is shown by error bars.

[64] Figure 8 (top) examines correlations when all time series are band-pass filtered to isolate 2–7 year variations. Here the ERA-Interim data show the strongest correlation to observations in all three Earth rotation components, while ERA-40 data only show significant correlations for $\chi_3$, presumably due to the more sparse data assimilation in ERA-40 prior to the satellite age. OAM excitation is only found to be statistically significant for $\chi_2$ variations, and HAM excitation is found to be significant nowhere. To the extent that the ERA-Interim data can be considered our best possible estimate of the true atmospheric excitation, we can say that the atmosphere dominates interannual variations not just in $\chi_3$, where the connection between atmospheric dynamics and $\Delta$LOD is fairly well known, but also in $\chi_1$ and $\chi_2$. This suggests that non-axisymmetric interannual modes of atmospheric variability, such as the North Atlantic Oscillation, may have a significant effect on polar motion, which has also been suggested by *Chao and Zhou* [1999] and *de Viron et al.* [2001].

[65] In contrast to the ERA-Interim data, the four EMAC-FUB simulations show no really significant correlations to the observations in $\chi_1$ and $\chi_2$, and only the CCMVal simulation has a significant correlation to observations in $\chi_3$. The higher correlation in the CCMVal simulation is not surprising, since the CCMVal simulation has realistic SST and solar cycle boundary conditions, resulting in realistic ENSO events, whereas the EMAC-FUB simulations with climatological boundary conditions represent arbitrary years. Note the proximity of the correlations to observations of $\chi_3$ estimated for the CCMVal simulation to those estimated from ERA-40 and ERA-Interim. This implies that simply having correct boundary conditions already accounts for the majority of the interannual atmospheric excitation of $\Delta$LOD variations.

[66] Of course, the other three EMAC-FUB simulations are constrained to realistic interannual atmospheric variability in one way, namely the QBO forcing. The effect of this is examined in the bottom panel, which shows the correlations to the observations when the data are band-pass filtered to isolate 23–34 month, i.e. quasi-biennial, variations. In this case, all four EMAC-FUB simulations show clear correlation to the observations in $\chi_3$, and two simulations (EMAC42 and EMAC63) even have marginally-significant correlations for $\chi_1$ and $\chi_2$, though they are only slightly within the 95% confidence interval.

### 3.5. Long-Term Variations (>7 Years)

[67] Significant decadal and longer variations exist in both polar motion and $\Delta$LOD. Polar motion exhibits a circa 30-year variation called the Markowitz wobble, along with a linear drift attributed to glacial isostatic adjustment and sea level changes [*Gross et al.*, 2005, and references therein]. *Gross et al.* [2005] showed that the atmosphere and ocean together only supply about 20–30% of decadal polar motion excitation, which leaves the majority of decadal polar motion variations largely unexplained. We therefore focus only briefly on long-term variations in $\Delta$LOD.

[68] By examining coherence between decadal LOD fluctuations and $\chi_3$, *de Viron et al.* [2004] showed that the atmosphere accounts for about 20% of the 13–14-year variations in $\Delta$LOD. *Salstein and Rosen* [1986] have suggested that decadal variations in observed $\Delta$LOD may serve as a proxy measure of long-term climate change. Observed $\Delta$LOD and AAM also seem to exhibit 11- and 22-year

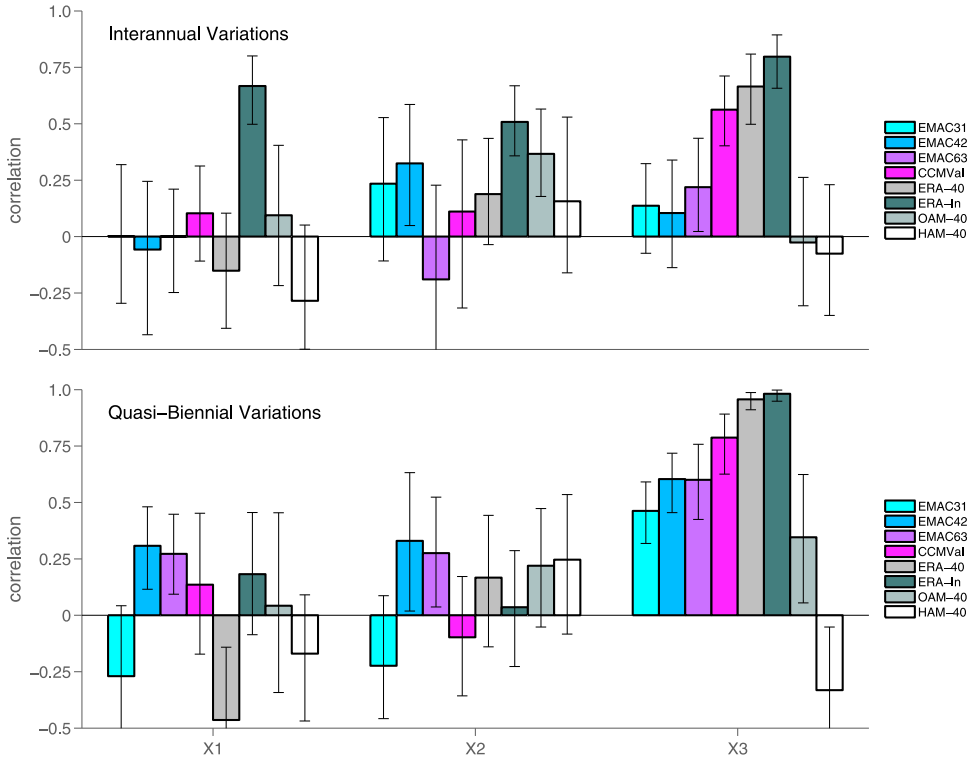


**Figure 8.** Correlations between the observed ERPs ($p_1$, $p_2$, and $\Delta$LOD) and their corresponding excitation functions ($\chi_1$, $\chi_2$, and $\chi_3$, respectively), estimated from the data sets described in Table 1. Correlations are estimated using a 1000-sample bootstrap algorithm. The mean correlation in each case is indicated by a bar, and the 95% confidence interval by error brackets. (top) Band-pass filtering all timescales to allow only 2–7 year variations. (bottom) Band-pass filtering to isolate 23–34 month (quasi-biennial) oscillations.

variations, which may reflect an influence of the 11-year solar cycle on climate [*Jochmann and Greiner-Mai*, 1996; *Abarca del Rio et al.*, 2003] though the mechanisms for this are not yet clear.

[69] Besides the hydrospheric excitation sources, long-timescale $\Delta$LOD variations are also excited by angular momentum exchange between the Earth's core and mantle [*Jochmann and Greiner-Mai*, 1996; *Greiner-Mai and Jochmann*, 1998]. This excitation source must also be subtracted from the observations when evaluating the atmospheric footprint on decadal and longer Earth rotation variations. Figure 9a shows the unfiltered time series of observed $\Delta$LOD fluctuations from 1962 to 2008. The time series is compared to an estimate of axial excitation due to core-mantle coupling angular momentum (CAM), estimated by J. Hagedoorn (personal communication, 2011) from the geomagnetic field model C3FM2 [*Wardinski and Holme*, 2006]. With no lag, the CAM $\chi_3$ time series has a correlation of about 0.38 with the corresponding $\Delta$LOD. Estimating a decorrelation time of about three years for these variations, correlation of about 0.55 can be considered significant at the 95% level according to a Student's t-test. Figure 9b shows the residual excitation after the CAM time series has been subtracted from $\Delta$LOD, low-pass filtered to allow only periods longer than 7 years. The residual is compared to $\chi_3$ from the CCMVal simulation and ERA-40, similarly filtered. The correlations between the residual (OBS-CAM) and the ERA-40 and CCMVal $\chi_3$ time series are 0.35 and $-0.37$, respectively – too small to be considered significant.

[70] Assimilation of ERP observations on this timescale could conceivably investigate budget closure, perhaps by optimizing parameters in the atmospheric or core-mantle models, such that long-term LOD variations can be fully explained in a physical way. However, more accurate estimates of the effect of core-mantle coupling than are currently available would likely be needed for this, as well as a longer time series of accurate Earth rotation observations in order to achieve statistical significance.

## 4. Spatial Information in ERP Observations

[71] We now investigate the geographical regions to which the AEF variations shown above are most sensitive, for each timescale. This is intended to further illustrate how observations of ERPs may in the future be used to constrain atmospheric models. *Nastula et al.* [2009] investigated the relationships between local atmospheric variations and the global equatorial AEFs, by plotting the covariances between local contributions to the equatorials AEFs and their global values. We apply a similar analysis here, but now extending it to all three AEFs, and using the 40 years of daily fields in the CCMVal simulation as an ensemble of states. Note that the covariance matrices used to update the model variables at a given observation time in a formal data assimilation approach are typically not equal to climatological covariances such as we examine here. This section is primarily intended to shed light on the physical mechanisms that cause the atmospheric excitation of ERPs at each timescale.

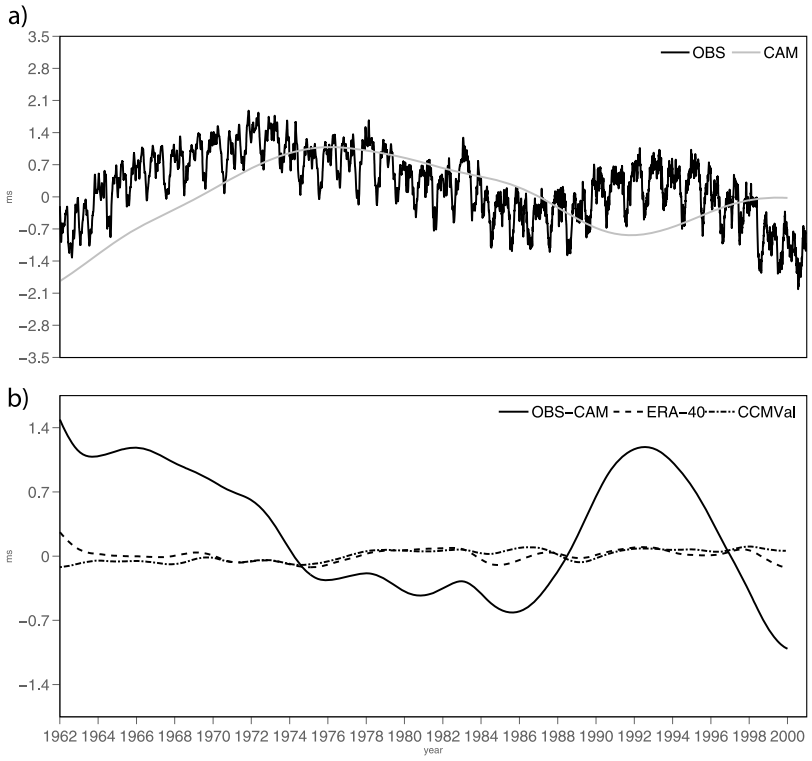


**Figure 9.** (a) Unfiltered time series of observed $\Delta$LOD, along with the excitation due to core-mantle interactions preliminarily estimated using a magnetic field model by J. Hagedoorn (personal communication, 2011). (b) The residual of observed $\Delta$LOD and the core-mantle excitation, compared to the geophysical AEFs estimated by the CCMVal simulation and ERA-40.

[72] Figures 10, 11, and 12 show maps of the estimated covariances between local contributions to the three AEF components and their global totals, for subseasonal (30–90 days, Figure 10), annual (230–450 days, Figure 11), and interannual (2–7 years, Figure 12) variations. As in the previous section, the covariances are estimated using a stationary bootstrap algorithm, though now only 500 bootstrap samples are taken in order to make the computation time feasible. All covariances that are not statistically different from zero at the 95% confidence level are masked out. As the application of the IB approximation causes spuriously large covariances to appear, covariances over ocean regions are masked out in the mass term plots (Figures 10a, 10b, 11a, 11c, and 12a). We have also omitted terms where the net global variation is very weak because regional contributions tend to cancel each other out in the global integral, i.e. the wind-terms of $\chi_1$ and $\chi_2$ on the subseasonal and interannual timescales [*Nastula et al.*, 2009; *Dobslaw et al.*, 2010], and the mass term of $\chi_3$ on all three timescales considered. The absolute values of the covariances are shown in order to focus on the main regions that affect the global AEFs, without considering the extra aspect of positive and negative contributions to the total, which depend on the signs of the transfer functions in the AEF integrals (illustrated in auxiliary material).

[73] Subseasonal variations in the mass terms of $\chi_1$ and $\chi_2$ (Figures 10a and 10b) look very similar to the corresponding plots from *Nastula et al.* [2009, Figure 3g]. The strongest influence comes from regions poleward of about $\pm 30°$, and longitudinal maxima are found where landmasses coincide with local maxima in the trigonometric weighting functions for these AEFs (equation (7)): Eurasia and Alaska for $\chi_1$, and central Siberia and northern North America for $\chi_2$. Subseasonal variations in $\chi_3$ (Figure 10c) are found to depend mostly on wind excitation throughout the tropics, which likely reflects the influence of the MJO in LOD variations, but fluctuations in the extratropical jets, over the North Atlantic and South Pacific, can also be seen.

[74] Local covariances are far stronger for all three components in the annual band (Figure 11), a result that was also found by *Nastula et al.* [2009] for the equatorial components. Here the wind term plays a much stronger role than mass in $\chi_1$ (compare Figures 11b and 11a), which was also seen in the sensitivity of the $\chi_1$ wind term to different model constraints in Figure 6b. The structure of the $\chi_2$ mass term (Figure 11c) is qualitatively similar to the analogous plot made by *Nastula et al.* [2009], revealing the effects of the wintertime high pressure systems that appear annually over Asia, South America, and Australia. An overall shift from high- to mid- and tropical latitudes can also be seen relative to the subseasonal band (Figure 10b), with local minima in the covariance around the edges of high-topography regions, e.g. the Rocky Mountains and the Tibetan Plateau.

[75] *Hide et al.* [1997] showed that annual variations in $\chi_3$ depend primarily on the annual variation of subtropical tropospheric jets; here this effect is seen in all three terms (Figures 11b, 11d, and 11f), with the effect in each component modulated by its respective zonal wind transfer

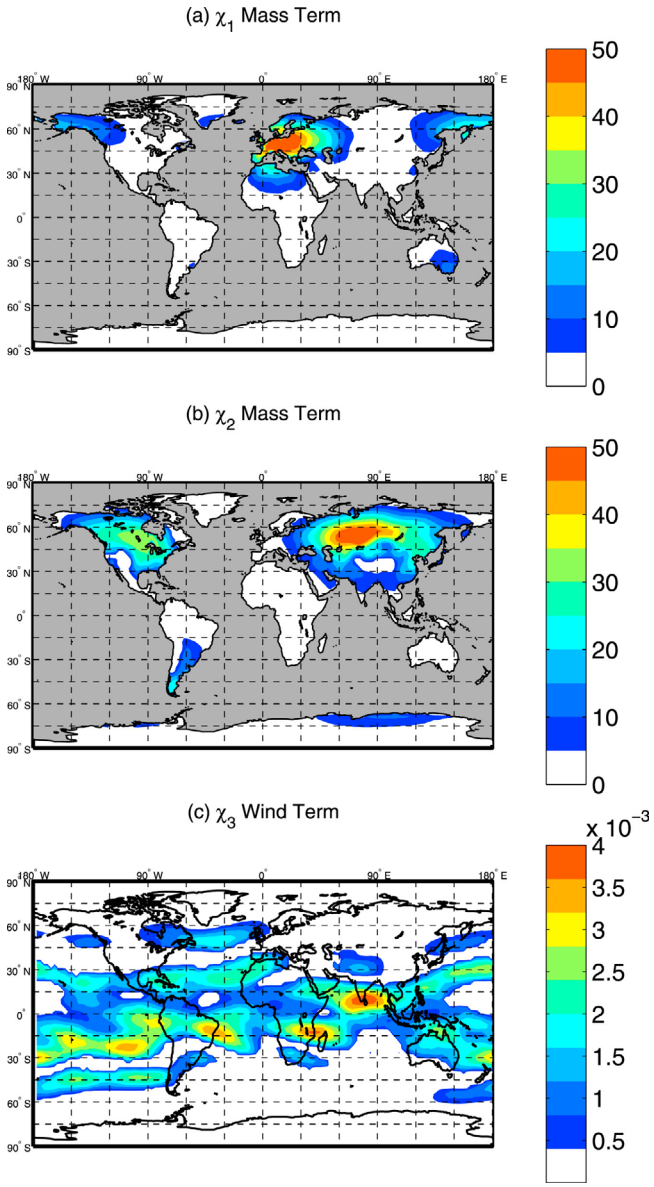


**Figure 10.** Absolute-value covariance between grid box contributions and the global values of the three AEFs. Only the mass contributions are shown for (a) $\chi_1$ and (b) $\chi_2$, while only the wind contribution is shown for (c) $\chi_3$ (see text). The covariances are computed from 40 years of daily data from the CCMVal simulation, which have been filtered to isolate subseasonal (30–90 d) variations.

functions. Contributions to the wind term of $\chi_3$ are largely axially symmetric, though a clear maximum is seen across the Eastern hemisphere.

[76] For interannual variations, the strongest significant local correlations were found for the mass term of $\chi_2$ and the wind term of $\chi_3$, shown in Figure 12. It can be seen that the spatial structure of these covariances is similar to the subseasonal timescale (Figures 10a and 10b), with atmospheric mass changes over Siberia and the western United States driving the interannual changes in $\chi_2$ and subtropical jet variations the interannual changes in $\chi_3$.

## 5. Conclusions

[77] We have evaluated the atmospheric excitation of three Earth rotation parameters, the two components of polar motion and anomalies in the length-of-day, comparing model simulations that were unconstrained by meteorological data to those produced by data-constrained simulations (reanalyses). This approach was similar to that of *Hide et al.* [1997], but included an emphasis on the effects of two other model constraints, QBO nudging and (in one case) time-dependent boundary conditions, and covered not just $\Delta$LOD, but all three observed ERPs. Atmospheric excitation functions computed geophysically from models were compared to the excitation implied by ERP observations, with the goal of identifying how the various model constraints affect the simulated Earth rotation observation, and in a more general sense, to identify the potential for the assimilation of ERPs as an additional constraint on atmospheric models. Here we summarize the main points found for polar motion observations (i.e., AEFs $\chi_1$ and $\chi_2$), and then for $\Delta$LOD variations (i.e., AEF $\chi_3$).

[78] It was found that polar motion, while not influenced as directly by the atmosphere as $\Delta$LOD, is significantly influenced by atmospheric mass redistribution and winds, especially at subseasonal to annual timescales. On the subseasonal timescale a large difference was found between the data-constrained and -unconstrained models (Figure 4). The atmospheric excitation of polar motion on this timescale was found to be most clearly connected to mass changes over the Northern Hemisphere continents at midlatitudes (Figures 10a and 10b).

[79] For the annual cycle in polar motion excitation, systematic differences were found between the observed ERPs and the geophysically-estimated AEFs (Figure 5), especially in the equatorial AEFs, which can perhaps be attributed to the excitation from OAM and HAM, though the angular momentum budget on this timescale has not yet been fully balanced [*Dobslaw et al.*, 2010]. The equatorial AEFs also showed disagreement between the different model simulations, the wind term of $\chi_1$ varying widely depending on model resolution, and with a much weaker annual cycle when winds are constrained by meteorological observations. The net annual cycle of $\chi_1$ was found to be sensitive to the modeled intensity and position of the Northern subtropical jets (Figure 11a).

[80] At interannual timescales and longer, significant correlations between polar motion variations and atmospheric equatorial angular momentum excitation were only found for the ERA-Interim reanalysis, implying that the atmosphere does play a strong part in interannual polar motion variations, but that this is generally not captured in models without data assimilation.

[81] However, a potential constraint offered by polar motion observations for an atmosphere model will be limited by the accuracy of the OAM and HAM estimates available, which in turn depends on model errors in the ocean and hydrological models used to estimate their angular momenta.

[82] Variations in $\Delta$LOD are much easier to connect to atmospheric dynamics, since atmospheric excitation dominates $\Delta$LOD fluctuations for timescales up to about 3 years. In fact, in the ERA-Interim reanalysis it is possible to almost completely balance the geophysical $\chi_3$ excitation and the

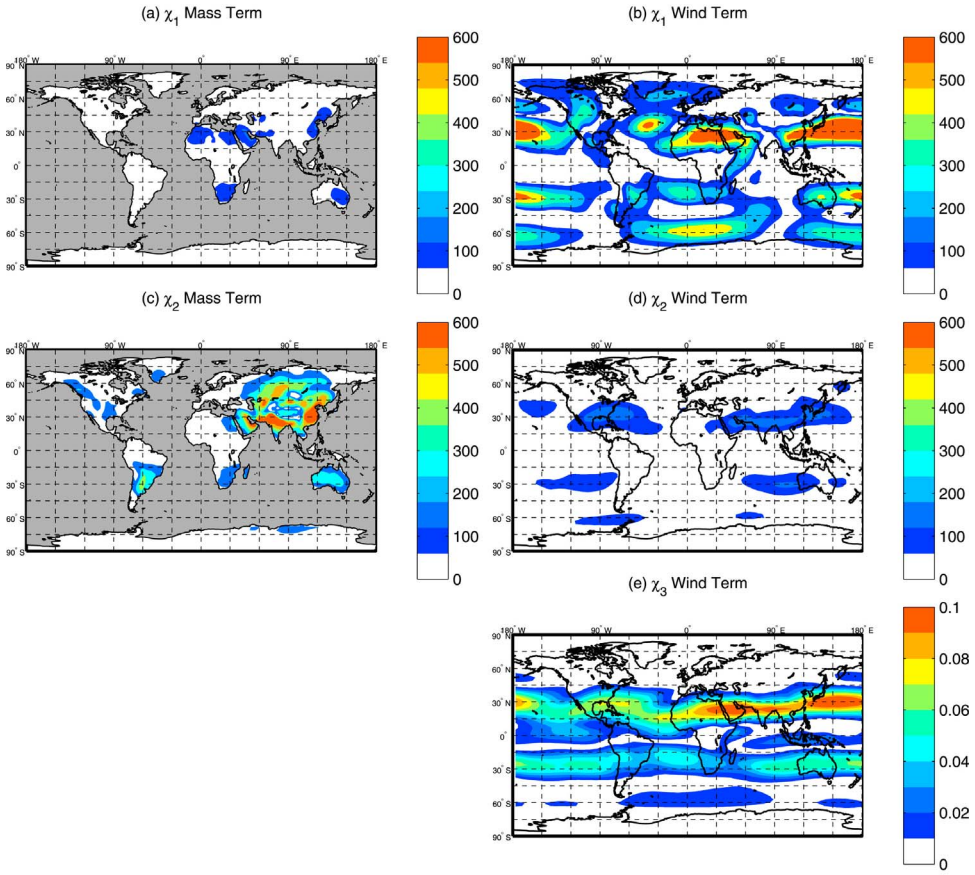


**Figure 11.** Absolute-value covariance between grid box contributions to all three AEFs, computed as in Figure 10, but now isolating annual (230–450 day) variations. Correlations for (a, c) the mass terms and (b, d, e) the wind terms of each component. Only the wind term is shown for $\chi_3$, as mass term covariances were found to be comparatively negligible.

observed $\Delta$LOD on subseasonal (Figure 4) and annual (Figure 5) timescales. For subseasonal variations, we speculate that constraining a model with $\Delta$LOD observations has the potential to constrain an otherwise-unconstrained atmosphere model in a way similar to "standard" meteorological variables, though this has yet to be tested. Here the continental hydrosphere was also found to be a small but significant source of $\Delta$LOD excitation, opposing the dominant atmospheric excitation. Since land hydrology models at present still return a wide range of excitation estimates (J. Nastula, personal communication, 2010), we defer the investigation of this to future work.

[83] As in previous studies, both variations in $\chi_3$ were found to depend primarily on subtropical wind variations, the subseasonal variations (Figure 10c) likely reflecting the MJO, the annual cycle the seasonal shift in the prevailing jets (Figure 11e) and in the interannual variations the ENSO phenomenon and, to a lesser extent, the QBO (Figure 12b). In contrast to subseasonal variations, the annual cycle in $\chi_3$ is captured similarly even in models that have no data

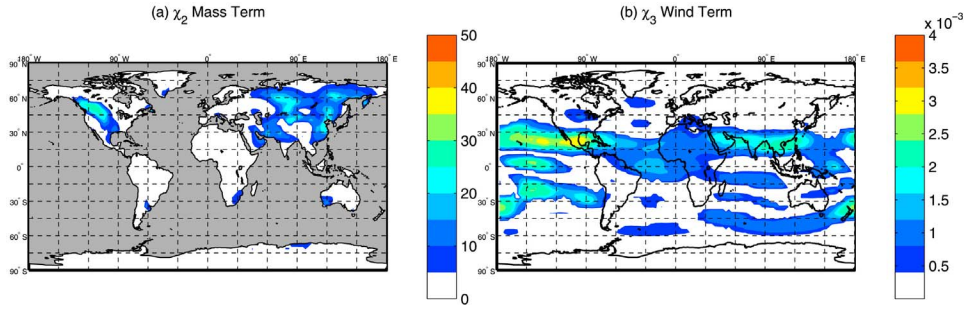


**Figure 12.** Absolute-value covariance between grid box contributions to (a) $\chi_2$ (mass contributions only) and (b) $\chi_3$ (wind contributions only), for interannual (2–7 year) variations.

assimilation and climatological boundary conditions (Figure 6c). Because interannual variations in ΔLOD excitation are primarily due to ENSO and the QBO, a large part of observed atmospheric excitation of ΔLOD fluctuations on this timescale were found to be captured with the CCMVal simulation, which contained a QBO and realistic boundary forcing.

[84] Regarding the possibility of using ERP observations as an additional model constraint, a major caveat to be remembered is that the observations represent integral measures of the wind and mass field in a modeled atmosphere. The model fields constitute a dynamical state of around $10^6$ degrees of freedom, i.e. vastly more than the three available observations. On the other hand, these observations are completely independent of meteorological observations, and are related to a globally-conserved quantity, the angular momentum of the Earth system. It remains to be seen how such a constraint can be intelligently applied to a model, despite the inherently underconstrained nature of the problem.

[85] A possible solution may be to localize the assimilation increment due to ERP observations in areas that are known to control certain ERP fluctuations, e.g. the Atlantic extratropical jet fluctuations that affect the annual cycle of $\chi_1$ (Figure 6b and auxiliary material). Another remedy might be to utilize ERP observations in concert with meteorological observations. Alternatively, one could imagine using ERP observations to adjust parameters in atmosphere, ocean, hydrosphere, and solid-Earth models in order to achieve budget closure in an optimal, physically-consistent way (as opposed to specifically improving modeled wind and pressure fields). One approach might be to adjust models of the continental hydrosphere, ocean, and atmosphere simultaneously in an Earth system model framework where all components are dynamically linked, in order to close the total angular momentum budget.

[86] **Acknowledgments.** This work has been performed within the Helmholtz-University Young Investigators Group NATHAN, funded by the Helmholtz-Association through the President's Initiative and Networking Fund, the GFZ Potsdam, and by the Freie Universität Berlin. The model calculations have been performed at the Deutsches Klimarechenzentrum (DKRZ), Hamburg, Germany. Henryk Dobslaw, provided AAM excitation functions from ERA-40 and ERA-Interim data, as well as OAM, and HAM excitation functions from OMCT and LSDM model simulations. Jan Hagedoorn provided the core-mantle excitation data. We would like to thank Henryk Dobslaw, Maik Thomas, Jolanta Nastula, and three anonymous reviewers for insightful comments and discussion that greatly improved this manuscript.

## References

Abarca del Rio, R., D. Gambis, D. Salstein, P. Nelson, and A. Dai (2003), Solar activity and earth rotation variability, *J. Geodyn.*, *36*, 423–443.

Anderson, J. R., and R. D. Rosen (1983), The latitude-height structure of the 40–50 day variation in atmospheric angular momentum, *J. Atmos. Sci.*, *40*, 1584–1591.

Barnes, R. T. H., R. Hide, A. White, and C. A. Wilson (1983), Atmospheric angular momentum fluctuations, length-of-day changes and polar motion, *Proc. R. Soc., Ser A*, *387*, 31–73.

Bizouard, C., and L. Seoane (2010), Atmospheric and oceanic forcing of the rapid polar motion, *J. Geod.*, *19*, 19–30.

Celaya, M. A., J. M. Wahr, and F. O. Bryan (1999), Climate-driven polar motion, *J. Geophys. Res.*, *104*, 12,813–12,829.

Chao, B., and Y.-H. Zhou (1999), Meteorological excitation of interannual polar motion by the North Atlantic Oscillation, *J. Geodyn.*, *27*, 61–73.

Chao, F. (1989), Length-of-day variations caused by El Niño–Southern Oscillation and quasi-biennial oscillation, *Science*, *243*, 923–925.

Chen, W., and W. Shen (2010), New estimates of the inertia tensor and rotation of the triaxial nonrigid Earth, *J. Geophys. Res.*, *115*, B12419, doi:10.1029/2009JB007094.

de Viron, O., S. L. Marcus, and J. O. Dickey (2001), Atmospheric torques during the winter of 1989: Impact of ENSO and NAO positive phases, *Geophys. Res. Lett.*, *28*, 1985–1988.

de Viron, O., D. Salstein, C. Bizouard, and L. Fernandez (2004), Low-frequency excitation of length of day and polar motion by the atmosphere, *J. Geophys. Res.*, *109*, B03408, doi:10.1029/2003JB002817.

Dickey, J. O., M. Ghil, and S. L. Marcus (1991), Extratropical aspects of the 40–50 day oscillation in length-of-day and atmospheric angular momentum, *J. Geophys. Res.*, *96*, 22,643–22,658.

Dickey, J. O., S. L. Marcus, and T. M. Chin (2007), Thermal wind forcing and atmospheric angular momentum: Origin of the Earth's delayed response to ENSO, *Geophys. Res. Lett.*, *34*, L17803, doi:10.1029/2007GL030846.

Dickey, J. O., S. L. Marcus, and O. de Viron (2010), Closure in the Earth's angular momentum budget observed from subseasonal periods down to four days: No core effects needed, *Geophys. Res. Lett.*, *37*, L03307, doi:10.1029/2009GL041118.

Dill, R. (2009), Hydrological model LSDM for operational Earth rotation and gravity field variations, *Sci. Tech. Rep. 08/09*, Dtsch. GeoForschungs., Potsdam, Germany.

Dobslaw, H., R. Dill, A. Grötsch, A. Brzezinski, and M. Thomas (2010), Seasonal polar motion excitation from numerical models of atmosphere, ocean, and continental hydrosphere, *J. Geophys. Res.*, *115*, B10406, doi:10.1029/2009JB007127.

Eubanks, T., J. Steppe, J. Dickey, and P. Callahan (1985), A spectral analysis of the Earth's angular momentum budget, *J. Geophys. Res.*, *90*, 5385–5404.

Giorgetta, M., E. Manzini, E. Roeckner, M. Esch, and L. Bengtsson (2006), Climatology and forcing of the quasi-biennial oscillation in the MAECHAM5 model, *J. Clim.*, *19*, 3882–3901.

Greiner-Mai, H., and H. Jochmann (1998), Correction to 'Climate variations and the Earth's rotation,' *J. Geodyn.*, *25*, 1–4.

Gross, R. S. (1992), Correspondence between theory and observations of polar motion, *Geophys. J. Int.*, *109*, 162–170.

Gross, R. S. (2009), Earth rotation variations—Long period, in *Geodesy, Treatise on Geophysics*, edited by T. Herring, pp. 239–294, Elsevier, New York.

Gross, R. S., I. Fukumori, and D. Menemenlis (2003), Atmospheric and oceanic excitation of the Earth's wobbles during 1980–2000, *J. Geophys. Res.*, *108*(B8), 2370, doi:10.1029/2002JB002143.

Gross, R. S., I. Fukumori, and D. Menemenlis (2005), Atmospheric and oceanic exciation of decadal-scale Earth orientation variations, *J. Geophys. Res.*, *110*, B09405, doi:10.1029/2004JB003565.

Hide, R., J. Dickey, S. Marcus, R. Rosen, and D. Salstein (1997), Atmospheric angular momentum fluctuations during 1979–1988 simulated by global circulation models, *J. Geophys. Res.*, *102*, 16,423–16,438.

Hines, C. (1997), Doppler-spread parametrization of gravity wave momentum deposition in the middle atmosphere. Part 2: Broad and quasi monochromatic spectra, and implementation, *J. Atmos. Sol. Terr. Phys.*, *59*, 387–400.

Jochmann, H., and H. Greiner-Mai (1996), Climate variations and the Earth's rotation, *J. Geodyn.*, *21*, 161–176.

Jöckel, P., et al. (2006), The atmospheric chemistry general circulation model ECHAM/MESSy1: Consistent simulation of ozone from the surface to the mesosphere, *Atmos. Chem. Phys.*, *6*, 5067–5104.

Le Mouël, J.-L., E. Blanter, M. Shnirman, and V. Courtillot (2010), Solar forcing of the semi-annual variation of length-of-day, *Geophys. Res. Lett.*, *37*, L15307, doi:10.1029/2010GL043185.

Manzini, E., and N. A. McFarlane (1998), The effect of varying the source spectrum of a gravity wave parametrization in a middle atmosphere general circulation model, *J. Geophys. Res.*, *103*, 31,523–31,539.

Morgenstern, O., et al. (2010), Review of the formulation of present-generation stratospheric chemistry climate models and associated external forcings, *J. Geophys. Res.*, *115*, D00M02, doi:10.1029/2009JD013728.

Mudelsee, M. (2003), Estimating pearson's correlation coefficient with bootstrap confidence interval from serially dependent time series, *Math. Geol.*, *35*, 651–665.

Nastula, J., D. Salstein, and B. Kolaczek (2009), Patterns of atmospheric excitation functions of polar motion from high-resolution regional sectors, *J. Geophys. Res.*, *114*, B04407, doi:10.1029/2008JB005605.

Nissen, K., K. Matthes, U. Langematz, and B. Mayer (2007), Towards a better representation of the solar cycle in general circulation models, *Atmos. Chem. Phys.*, *7*, 5391–5400.

Proakis, J., and D. Manolakis (1996), *Digital Signal Processing: Principles, Algorithms, and Applications*, 481 pp., Prentice-Hall, Upper Saddle River, N. J.

Rosen, R. D., and D. A. Salstein (1983), Variations in atmospheric angular momentum on global and regional scales and the length of day, *J. Geophys. Res.*, *88*, 5451–5470.

Rosen, R. D., and D. A. Salstein (2000), Multidecadal signals in the interannual variability of atmospheric angular momentum, *Clim. Dyn.*, *16*, 693–700.

Rosen, R. D., D. A. Salstein, and T. M. Wood (1991), Zonal contributions to global momentum variations on intraseasonal through interannual timescales, *J. Geophys. Res.*, *96*, 5145–5151.

Salstein, D. A., and R. D. Rosen (1986), Earth rotation as a proxy for interannual variability in atmospheric circulation, 1860-present, *J. Clim. Appl. Meteorol.*, *25*, 1870–1877.

Salstein, D. A., and R. D. Rosen (1989), Regional contributions to the atmospheric excitations of rapid polar motions, *J. Geophys. Res.*, *94*, 9971–9978.

Sander, R., A. Kerkweg, P. Jöckel, and J. Lelieveld (2005), Technical note: The new comprehensive atmospheric chemistry module MECCA, *Atmos. Chem. Phys.*, *5*, 445–450.

SPARC CCMVal (2010), SPARC report on the evaluation of chemistry-climate models, *SPARC Rep. 5*, SPARC CCMVal, U. Toronto, Toronto, Ont., Canada. [Available at http://www.atmosp.physics.utoronto.ca/SPARC.]

Thomas, M. (2002), Ocean induced variations of Earth's rotation–Results from a simultaneous model of global circulation and tides, PhD thesis, 129 pp., Univ. of Hamburg, Hamburg, Germany.

Thomas, M., J. Sündermann, and E. Maier-Reimer (2001), Consideration of ocean tides in an OGCM and impacts on subseasonal to decadal polar motion excitation, *Geophys. Res. Lett.*, *28*(12), 2457–2460, doi:10.1029/2000GL012234.

Uppala, S. M., et al. (2005), The ERA-40 re-analysis, *Q. J. R. Meteorol. Soc.*, *131*(612), 2961–3012, doi:10.1256/qj.04.176.

Uppala, S., D. Dee, S. Kobayashi, P. Berrisford, and A. Simmons (2008), Towards a climate data assimilation system: status update of ERA Interim, *ECMWF Newsl.*, *115*, 12–18.

Wardinski, I., and R. Holme (2006), A time-dependent model of the Earth's magnetic field and its secular variation for the period 1980–2000, *J. Geophys. Res.*, *111*, B12101, doi:10.1029/2006JB004401.

Wunsch, C., and D. Stammer (1997), Atmospheric loading and the oceanic "inverted barometer" effect, *Rev. Geophys.*, *35*(1), 79–107.

Yu, N., D. Zheng, and H. Wu (1999), Contribution of new AAM data source to ΔLOD excitation, *J. Geod.*, *73*, 385–390.

Zhao, J., and W. Qu (1995), Study of the dynamical mechanism of seasonal variation of Earth's rotational velocity, *J. Geophys. Res.*, *100*, 12,719–12,730.

K. Matthes and L. J. Neef, GFZ German Research Centre for Geosciences, Section 1.3, Earth System Modeling, Telegrafenberg, A20 323, D-14473 Potsdam, Germany. (neef@gfz-potsdam.de)